

Inverse-designed photonics for semiconductor foundries

Alexander Y. Piggott,^{†,§} Eric Y. Ma,^{†,‡,§} Logan Su,^{†,§} Geun Ho Ahn,[†] Neil V. Sapro,[†] Dries Vercruysse,[†] Andrew M. Netherton,[¶] Akhilesh S.P. Khope,[¶] John E. Bowers,[¶] and Jelena Vučković^{*,†}

[†]*Ginzton Laboratory, Stanford University, Stanford, CA, USA*

[‡]*Stanford Institute for Materials and Energy Sciences, SLAC National Accelerator Laboratory, Menlo Park, CA, USA*

[¶]*University of California Santa Barbara, Santa Barbara, CA, USA*

[§]*These authors contributed equally to the work.*

E-mail: jela@stanford.edu

Abstract

Silicon photonics is becoming a leading technology in photonics, displacing traditional fiber optic transceivers and enabling new applications. Further improving the density and performance of silicon photonics, however, has been challenging, due to the large size and limited performance of traditional semi-analytically designed components. Automated optimization of photonic devices using inverse design is a promising path forward but has until now faced difficulties in producing designs that can be fabricated reliably at scale. Here we experimentally demonstrate four inverse-designed devices - a spatial mode multiplexer, wavelength demultiplexer, 50-50 directional coupler, and 3-way power splitter - made successfully in a commercial silicon photonics foundry. These devices are efficient, robust to fabrication variability, and compact,

with footprints only a few micrometers across. They pave the way forward for the widespread practical use of inverse design.

Keywords: *Nanophotonics, silicon photonics, inverse design, foundry fabrication*

Silicon photonics is becoming a leading technology in photonics¹ by displacing traditional photonics and enabling new applications in a wide variety of product areas. For example, silicon photonic transceivers are quickly becoming the de-facto standard for fiber optics links, ranging from long-haul telecommunications to intra-data-center links.² New applications such as LiDAR (Light Detection And Ranging)^{3,4} and optical machine learning^{5,6} are actively being developed. The key to the success of silicon photonics is that it leverages standard CMOS (Complementary Metal Oxide Semiconductor) fabrication processes, allowing high-performance optical systems to be produced in large volumes at very low cost.^{6,7}

Progress in silicon photonics, however, has long been hampered by the small library of semi-analytically designed devices in common use. These traditional designs are rather large, ranging from tens to hundreds of microns in size for even basic functions, and often leave much to be desired in terms of performance and robustness. A promising solution is inverse design, whereby photonic devices are designed by optimization algorithms with little-to-no human input.⁸⁻¹⁷ Inverse design has successfully produced designs that have improved optical performance, improved robustness to errors in fabrication and variation of operational conditions, or use orders of magnitude less area, when compared to previous designs. Such compact devices are especially useful for newer applications of silicon photonics that require high photonic component densities, such as phased arrays for LiDAR systems and dense arrays of Mach-Zehnder interferometers for machine learning. Unfortunately, the devices generated by inverse design often have small features that are difficult to fabricate reliably using photolithography, the mainstay of commercial semiconductor manufacturing. Indeed, the vast majority of previous experimental demonstrations of inverse-designed photonics have used either electron-beam lithography or focused ion beam machining, which have considerably higher resolution but cannot be used to produce devices at scale.^{9,13,14,18-20}

There are a few demonstrations using photolithography, but they unnecessarily restrict the design space and cannot handle arbitrary topologies.^{21,22} To the best of our knowledge, the only previous attempt at fabricating inverse-designed devices at a foundry had poor agreement between simulated and experimental performance due to significant differences between the designed and fabricated structures.²²

In this work, we report the first successful demonstration of inverse-designed photonics in a commercial silicon photonics process. The designs were fabricated as part of the AIM Photonics 300 mm wafer multi-project wafer (MPW) foundry offering.²³ We demonstrate four different devices fabricated using a single fully-etched layer of 220 nm thick silicon, surrounded on all sides by silicon dioxide cladding. These devices are compact, with footprints of only several micrometers across, and have comparable performance and reproducibility to previous inverse-designed devices fabricated using electron-beam lithography (Fig. 1).

Results

Design

The goal of inverse design is to automate the design process. First, a human designer broadly specifies the desired performance and other characteristics of the device, such as the desired transmission through an output port with a given design area.^{18,19,24} An optimization algorithm is then used to search the space of available designs using gradient-based optimization, which can efficiently optimize over tens or even hundreds of thousands of design degrees of freedom. By using adjoint sensitivity analysis, the gradient can be efficiently computed using one additional electromagnetic simulation, regardless of the number of design parameters.^{12,24–26}

To successfully fabricate devices at a foundry, the designs should be robustly resolved using photolithography. In principle, it would be possible to directly incorporate a lithography model into the optimization algorithm, but this requires detailed knowledge of the lithogra-

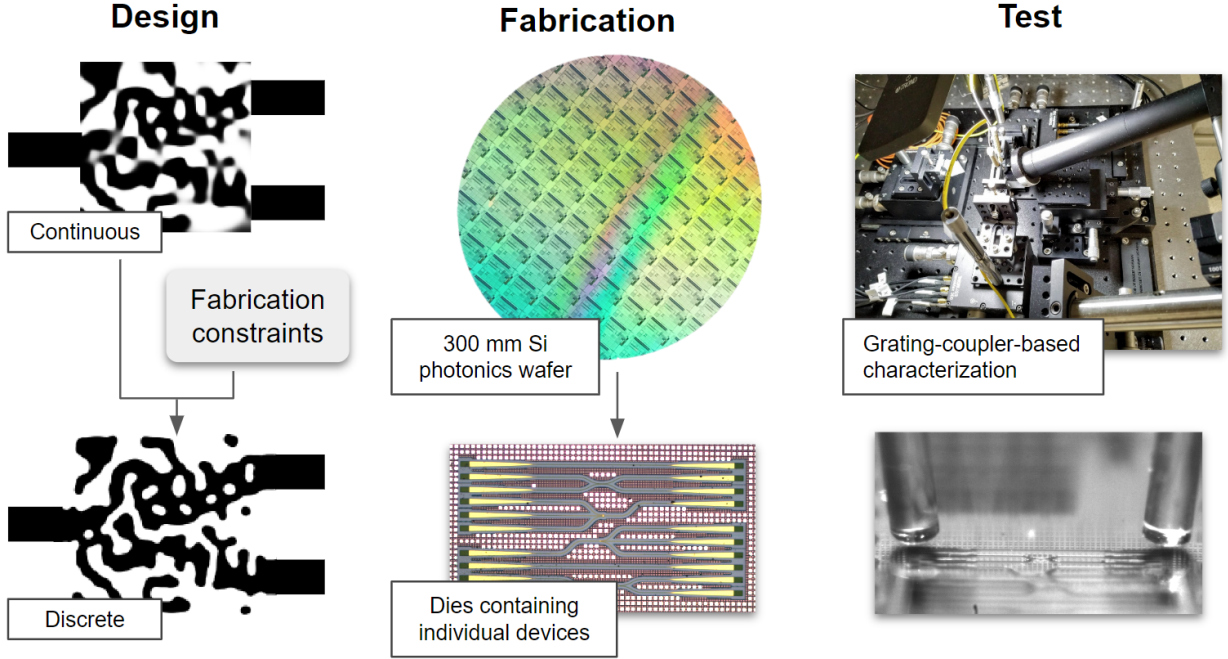


Figure 1: Workflow of photonics inverse design for commercial silicon photonics foundries. Fabrication constraints are applied in the discrete optimizations. The final device design is then combined with components from the foundry’s PDK (Process Design Kit), e.g. waveguides and grating couplers, to complete the final mask pattern. AIM Photonics 300 mm multi-project Si wafers are then fabricated via water-immersion deep UV photolithography at the Albany NanoTech fabrication facility. The wafer is diced and the devices tested in a vertical transmission measurement setup. (*Wafer image by Frank Tolic. Other photos taken by authors.)

phy parameters used by the foundry. In lieu of directly incorporating a lithography model,¹⁸ proposed using two constraints as heuristics: a minimum gap and a minimum radius of curvature. More specifically, a minimum radius of curvature constraint is applied to all material interfaces, preventing the formation of any sharp cusps and corners. A minimum gap constraint prevents the formation of narrow gaps and bridges. To ensure robustness to fabrication errors, all devices were designed to operate over as broad of a range of wavelengths as possible, which has previously been shown to be an effective heuristic for fabrication robustness. As will be demonstrated through the experimental measurements, these two fabrication constraints, along with broadband optimization, are sufficient for creating devices that can be reliably fabricated at commercial foundries.

Spatial mode multiplexer

First we consider a compact spatial mode multiplexer, which separates the fundamental TE_{00} and second-order TE_{10} modes of a 750 nm wide multi-mode input waveguide, and routes them to separate 400 nm wide single-mode output waveguides (Fig. 2(a)). The device was designed by first allowing the permittivity in the design region to continuously vary between that of silicon and silicon dioxide, before applying thresholding and switching to boundary optimization.¹⁸ During boundary optimization, a 70 nm minimum radius of curvature and 90 nm minimum gap constraint were applied. This resulted in a design with a complex and non-intuitive topology and a compact footprint of $3.55 \times 2.55 \mu\text{m}^2$ (Fig. 2(b, c)).

To test the spatial mode multiplexer, two multiplexers were placed back-to-back, joined by an 80 μm segment of multi-mode waveguide. This allowed the device to be measured using standard single-mode optical fibers and grating couplers. Fig. 2(d) and (e) show that the simulated and measured S-parameters agree well with each other. In addition, the fabricated devices are very reproducible: the S-parameters of the three instances from three dies are closely aligned. Extracting the S-parameters of a single device is straightforward (Methods): over the entire operating bandwidth of 1500 – 1600 nm, the insertion loss is

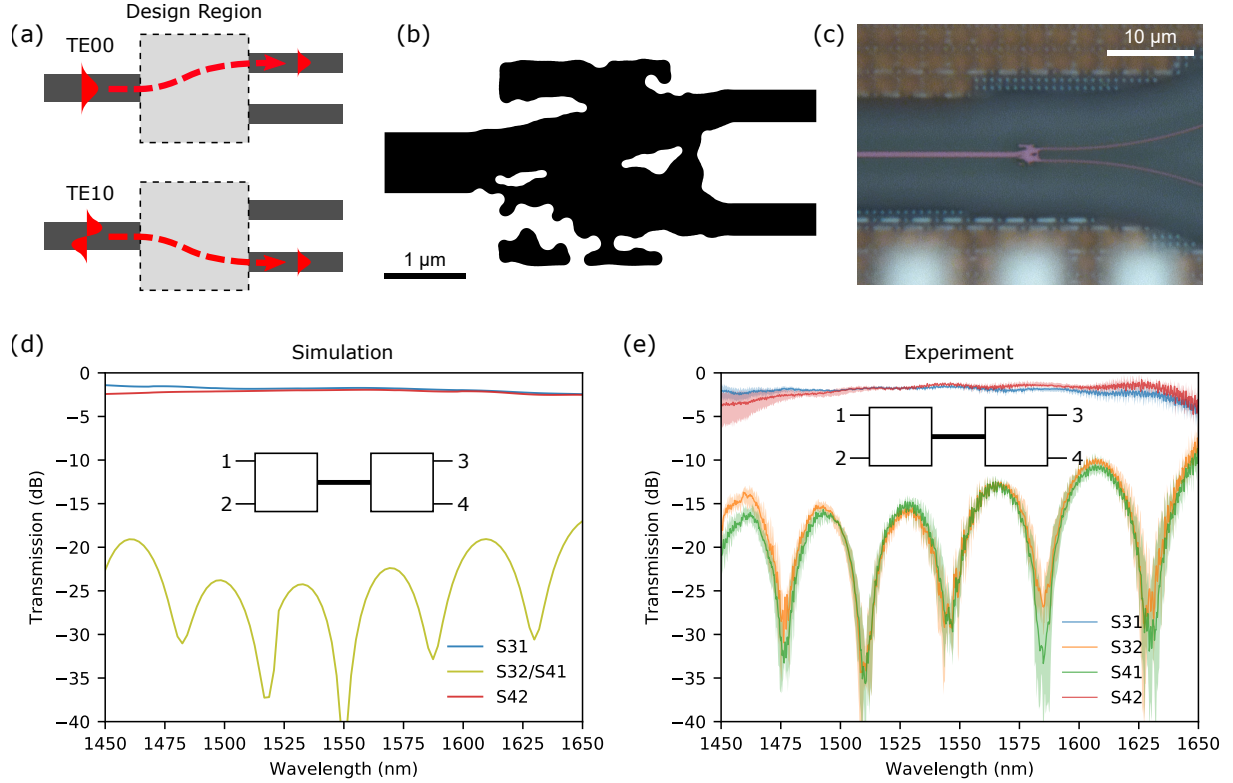


Figure 2: A spatial mode multiplexer. (a) The spatial mode multiplexer maps the TE₀₀ and TE₁₀ modes of the 750 nm wide input waveguide to the TE₀₀ mode of the two 400 nm wide output waveguides. (b) The final design, with regions of silicon indicated by black, and silicon dioxide indicated by white. (c) An optical microscopy image of the final fabricated device. (d) Simulated and (e) experimentally measured S-parameters for the back-to-back test structure that allows the design to be measured using only standard single-mode optical waveguides. The shaded areas in (e) indicate the minimum and maximum values across three different measured devices from three dies, and the solid lines the average.

< 1.0 dB, and the crosstalk suppression is > 15.6 dB.

Wavelength demultiplexer

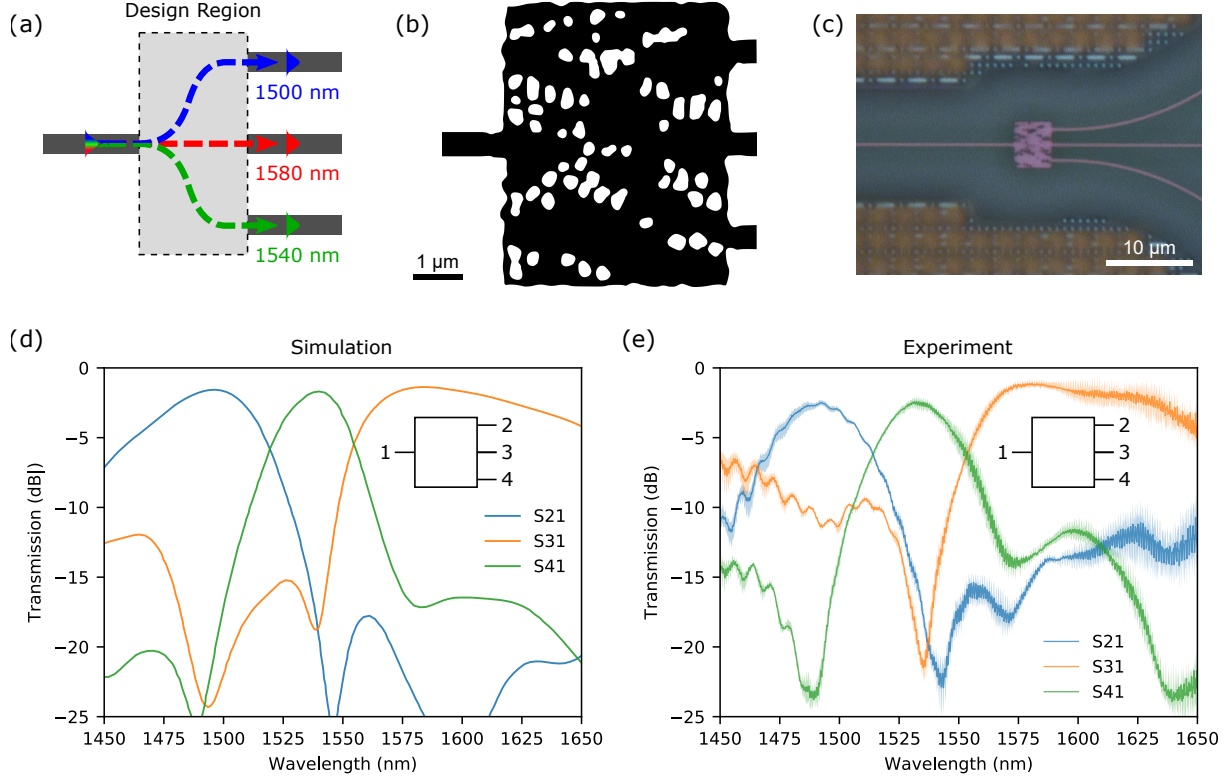


Figure 3: A 3-channel wavelength demultiplexer. (a) The wavelength demultiplexer splits 1500 nm, 1540 nm, and 1580 nm light into three separate output waveguides. (b) The final design, with regions of silicon indicated by black, and silicon dioxide indicated by white. (c) An optical microscopy image of the final fabricated device. (d) Simulated and (e) experimentally measured S-parameters for the wavelength demultiplexer. The shaded areas in (e) indicate the minimum and maximum values across three different measured devices. The three pass-bands at 1500 nm, 1540 nm, and 1580 nm are clearly visible in the data.

Next we consider a 3-channel wavelength demultiplexer, designed to separate 1500 nm, 1540 nm, and 1580 nm light (Fig. 3(a)). We used “neighbour biasing” in the continuous stage of optimization to produce a good starting point for boundary optimization.¹⁹ The minimum radius of curvature was 40 nm, and the minimum gap width was 90 nm. The design (Fig. 3(b, c)) is highly non-intuitive but compact, with a footprint of only $5.5 \times 4.5 \mu\text{m}^2$.

The simulated and measured S-parameters are presented in Fig. 3(d) and (e). The mea-

sured spectra exhibit three clear passbands, showing that the device functions as intended, although the crosstalk is somewhat higher. The reproducibility is also excellent: the three fabricated instances have nearly identical transmission. The insertion loss for the 3 output channels are 3.0 dB at 1500 nm, 3.1 dB at 1540 nm, and 1.2 dB at 1580 nm. The crosstalk suppression are 8.3, 12.6 and 12.3 dB, respectively.

Directional coupler

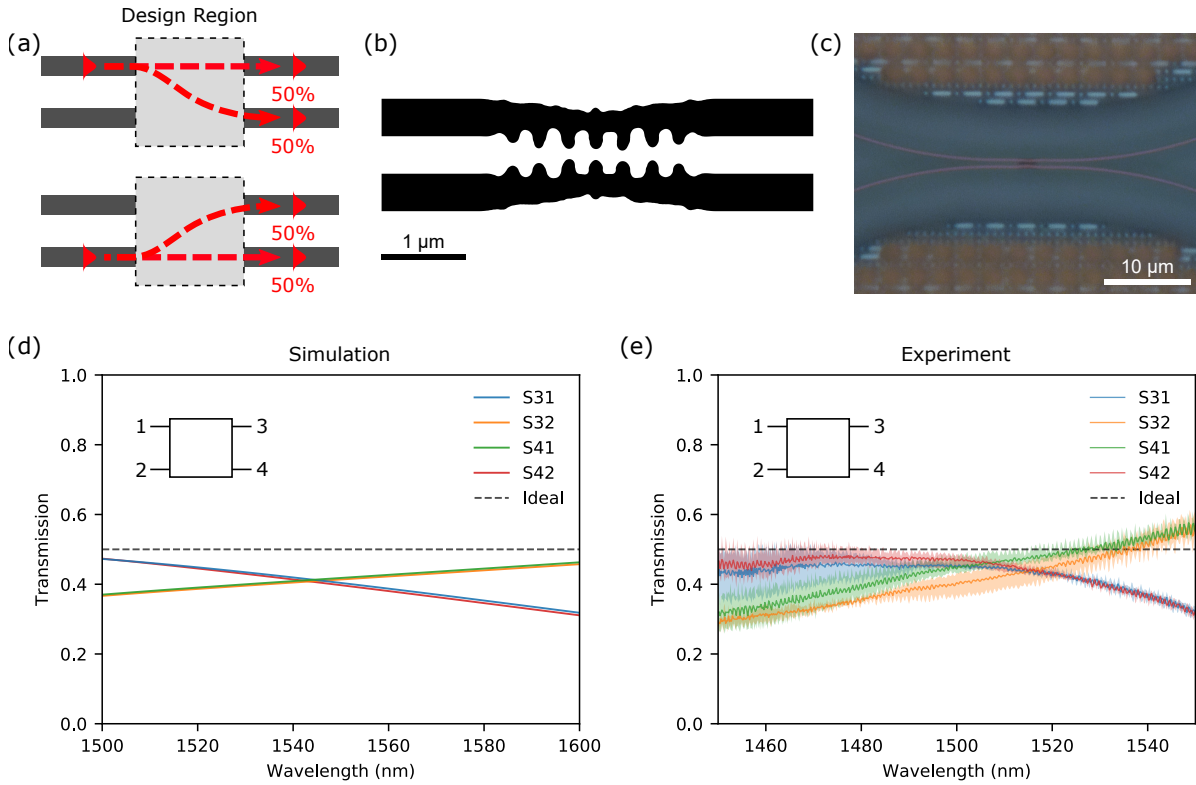


Figure 4: A 50-50 directional coupler. (a) A 50-50 directional coupler equally splits light from its two input waveguides into its two output waveguides. (b) The final design, with regions of silicon indicated by black, and silicon dioxide indicated by white. (d) Simulated and (e) experimentally measured performance of the directional coupler. The shaded areas in (e) indicate the minimum and maximum values across three different measured devices. The dashed line indicates a perfect 1/2 splitting ratio.

The third design is a 50-50 directional coupler that takes light from either of its two input waveguides and equally divides it between the two output waveguides (Fig. 4(a)). The same two-stage design process was used as for the spatial mode multiplexer, with minimum radius

of curvature of 70 nm and minimum gap of 90 nm. With a footprint of $3.0 \times 1.2 \mu\text{m}^2$, the final design is significantly more compact than most designs in the literature (Fig. 4(b)). Interestingly, the structure strongly resembles a conventional grating-assisted directional coupler, despite the complete lack of human intervention throughout the design process.

The design is relatively broadband, with reasonably matched output powers over a 100 nm bandwidth in both simulation (Fig. 4(d)) and measurement (Fig. 4(e)). Over a 45 nm bandwidth, the fabricated couplers have an average insertion loss of 0.5 dB and $< 10\%$ power imbalance. There is, however, a significant wavelength shift between the simulated and measured devices, likely due to fabrication errors: the design has a central wavelength of 1545 nm, whereas the measured devices operate around 1505 nm.

Power splitter

The last design is a broadband three-way power splitter that equally splits the power from an input waveguide into three output waveguides (Fig. 5(a)). In contrast to the previous designs, the power splitter was designed using only boundary optimization with minimum radius of curvature of 100 nm, yielding a design (Fig. 5(b)) that resembles a compact multi-mode interferometer (MMI) coupler.¹⁸ The final design has a footprint of $3.8 \times 2.5 \mu\text{m}$.

The simulated and measured S-parameters for the three-way power splitter are given in Fig. 5(d) and (e). The splitting is very broadband, operating nominally from 1450 nm to 1600 nm. The simulated and measured S-parameters match quite closely, although there is a shift in the transmission fringes. The design was constrained to have reflection symmetry across the horizontal axis, resulting in S_{12} and S_{14} parameters that are identical in simulation and nearly identical in measurement. Over the full operating bandwidth, the splitter has an insertion loss of 0.4 dB, and a power imbalance of 4.4%.

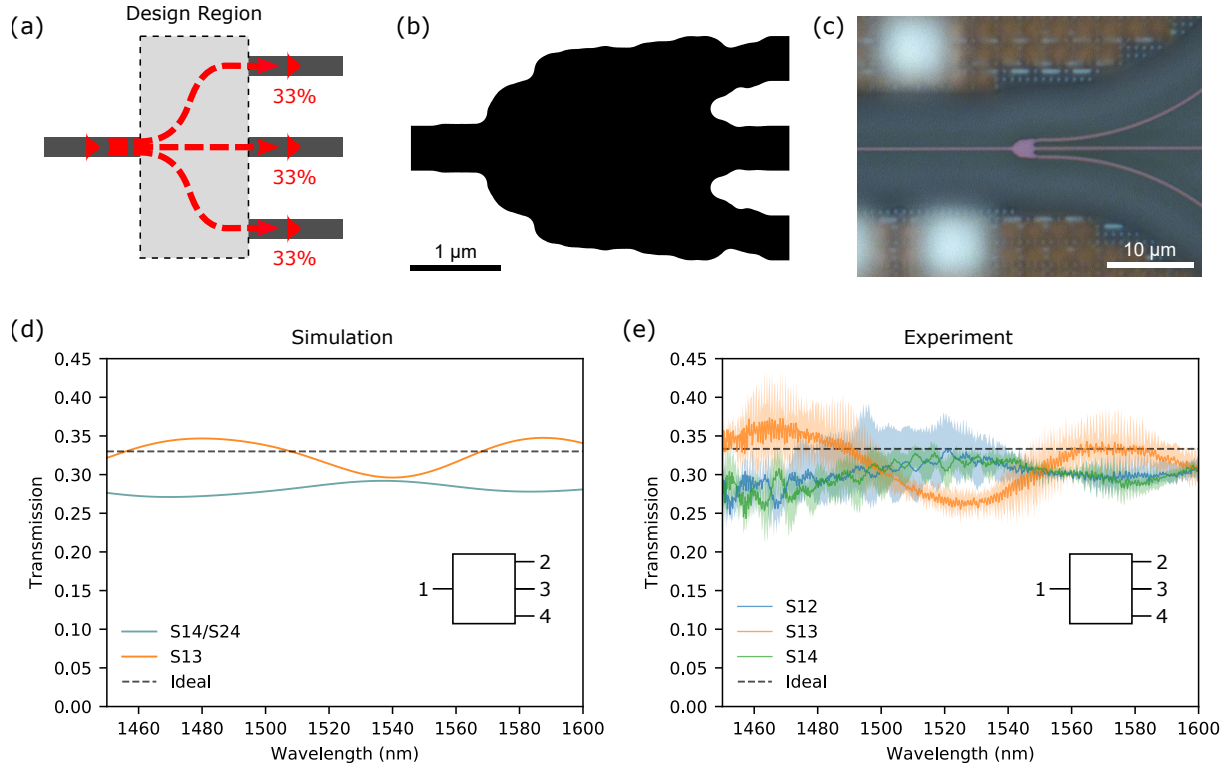


Figure 5: A 3-way power splitter. (a) The 3-way power splitter equally splits power between three output waveguides. (b) The final design, with regions of silicon indicated by black, and silicon dioxide indicated by white. (d) Simulated and (e) experimentally measured S-parameters for the 3-way power splitter. The shaded areas in (e) indicate the minimum and maximum values across three different measured devices. The dashed line indicates a perfect 1/3 splitting ratio.

Discussions

All four designs appear to be quite robust to fabrication errors. The device-to-device variability across the three dies, each containing a single instance of all designs, was approximately equal to our measurement uncertainty of ± 0.6 dB, limited mostly by grating coupler variability. This consistency suggests that they are robust to typical fabrication errors, such as defocusing in photolithography or variation in layer thicknesses. Furthermore, both the wavelength demultiplexer¹⁹ and 3-way power splitter¹⁸ were previously fabricated using electron-beam lithography and had comparable performance to the present devices. This implies that high-resolution electron-beam lithography is not necessary for fabricating these complex designs; industry-standard photolithography is sufficient, so long as the designs are properly constrained.

In summary, we have experimentally demonstrated a photonic inverse design process that is compatible with industry-standard photonics foundries. By incorporating fabrication constraints we have eliminated small features that cannot be resolved using photolithography. A wide breadth of devices were demonstrated, illustrating the flexibility of the method. These results show that inverse design is a suitable method for designing practical integrated photonic devices and has the potential to revolutionize the field by enabling a new generation of exceedingly compact and high performance devices.

Methods

Design algorithms

All devices were designed using our adjoint optimization based implementation of photonic inverse design.^{18,19,24} Our inverse design algorithm proceeds in two stages. In the first stage, the permittivity is allowed to continuously vary between those of the available materials (e.g. silicon and silicon dioxide) at every point in the design. The design is then thresholded to

produce a binary structure consisting of only two materials, which is used as the starting condition for the next stage. In the second stage, only the material boundaries are optimized by using a level set representation of the structure.²⁷ Under the level set representation, the boundary of the device is defined as the zero crossing of a continuous function.¹⁸ The implicit nature of the level set representation makes it trivial to handle changes in topology, such as the merging or splitting of holes, and does not require one to perform complex additional steps such as re-meshing.

The computational cost of inverse design is dominated by the required electromagnetic simulations, which were performed using Maxwell FDFD,^{28,29} a GPU-based implementation of the finite-difference frequency-domain (FDFD) method, with a spatial step size of 40 nm. The Maxwell FDFD simulation software is available on GitHub at <https://github.com/stanfordnqp/maxwell-b> under the GNU General Public License v3.0. Final broadband verification simulations were then performed using commercial Lumerical FDTD (finite-difference time-domain) software.³⁰ All simulations and design were performed on a server with an Intel Core i7-5820K processor, 64GB of RAM, and three Nvidia Titan Z graphics cards.

The spatial mode multiplexer, 3-way power splitter, and 50-50 directional coupler were optimized over 6 equally spaced wavelengths from 1400 nm to 1700 nm.¹⁸ This resulted in designs which operated well over a broad wavelength range. Meanwhile, the wavelength demultiplexer was optimized at the three channel wavelengths of 1500 nm, 1540 nm, and 1580 nm.¹⁹

Fabrication

As discussed in the main text, the designs were fabricated on an AIM Photonics 300 mm wafer multi-project wafer (MPW) run.²³ We waived the minimum width DRC (design-rule check) rule for the spatial mode multiplexer, 50-50 directional coupler, and wavelength demultiplexer, and waived the minimum separation rule for the spatial mode multiplexer and

wavelength demultiplexer. However, the designs were all successfully resolved by the 193 nm immersion lithography used in the AIM Photonics process, which can produce features as small as 40 nm across.³¹

Measurement

We measured the transmission through the devices by a home-built grating-coupling setup. The input and output fibers were mounted on flexure stages with piezo nanopositioners (Thorlabs NanoMax) and were 10 degrees from normal to the chip plane. We used a band-pass filtered supercontinuum laser (Fianium WhiteLase SC-400-4) as light source and an optical spectrum analyzer (Agilent 86140B) to measure the transmitted power spectra. The fibers were automatically aligned to maximize the transmitted power before each measurement. The power spectra of individual devices are reproducible to ± 0.5 dB. We obtain the transmission spectra of the devices by normalizing against the two straight waveguides on each chip. The transmission of these two straight waveguides have a variation of up to ± 0.6 dB on all three chips and we use the average spectra to normalize. In the figures containing experimental transmission data, the solid lines are the average spectra and the shaded regions the span of values from all three chips.

Extracting S-parameters for spatial mode demultiplexer

Extracting the S-parameters for a single multiplexer from the measured data is relatively straightforward. The S_{13} and S_{24} parameters of the back-to-back structure are a measure of insertion loss, and are equal to double the insertion loss of a single multiplexer. Meanwhile, the S_{14} and S_{32} parameters are measures of the crosstalk. In this test structure, there are two dominant crosstalk paths: light can be coupled into the wrong mode of the multi-mode waveguide by the first multiplexer, and light can be coupled into the wrong output waveguide by the second multiplexer. Since the TE_{00} and TE_{10} modes of the multi-mode waveguide have different propagation constants, this results in a fringing pattern in the S_{14} and S_{32}

spectra.

Acknowledgements

This work was supported by AIM Photonics, and sponsored by the Air Force Research Laboratory via agreement number FA8650-15-2-5220, the Air Force Office of Scientific Research MURI on Attojoule Optoelectronics via award number FA9550-17-1-0002, and the Gordon and Betty Moore Foundation via grant GBMF4744.

References

- (1) Mounie, E.; Malinge, J.-L. *Silicon Photonics and Photonic Integrated Circuits*; 2019.
- (2) Rahim, A.; Spuesens, T.; Baets, R.; Bogaerts, W. Open-Access Silicon Photonics: Current Status and Emerging Initiatives. *Proc. IEEE* **2018**, *106*, 2313–2330.
- (3) Sun, J.; Timurdogan, E.; Yaacobi, A.; Hosseini, E. S.; R. Watts, M. Large-scale nanophotonic phased array. *Nature* **2013**, *493*, 195 – 199.
- (4) Miller, S. A.; Phare, C. T.; Chang, Y.; Ji, X.; Gordillo, O. A. J.; Mohanty, A.; Roberts, S. P.; Shin, M. C.; Stern, B.; Zadka, M.; Lipson, M. 512-Element Actively Steered Silicon Phased Array for Low-Power LIDAR. 2018 Conference on Lasers and Electro-Optics (CLEO). 2018; pp 1–2.
- (5) Shen, Y.; Harris, N. C.; Skirlo, S.; Prabhu, M.; Baehr-Jones, T.; Hochberg, M.; Sun, X.; Zhao, S.; Larochelle, H.; Englund, D.; Soljačić, M. Deep learning with coherent nanophotonic circuits. *Nature Photonics* **2017**, *11*, 441.
- (6) Komljenovic, T.; Davenport, M.; Hulme, J.; Liu, A. Y.; Santis, C. T.; Spott, A.; Srinivasan, S.; Stanton, E. J.; Zhang, C.; Bowers, J. E. Heterogeneous silicon photonic integrated circuits. *Journal of Lightwave Technology* **2016**, *34*, 20–35.

- (7) Reed, G. T. *Silicon Photonics: The State of the Art*; John Wiley & Sons: Chichester, West Sussex, U.K., 2008.
- (8) Mutapcica, A.; Boyd, S.; Farjadpour, A.; Johnson, S. G.; Avnielb, Y. Robust design of slow-light tapers in periodic waveguides. *Eng. Optimiz.* **2009**, *41*, 365 – 384.
- (9) Jensen, J. S.; Sigmund, O. Topology optimization for nano-photonics. *Laser Photonics Rev.* **2011**, *5*, 308 – 321.
- (10) Lalau-Keraly, C. M.; Bhargava, S.; Miller, O. D.; Yablonovitch, E. Adjoint shape optimization applied to electromagnetic design. *Opt. Express* **2013**, *21*, 21693 – 21701.
- (11) Lu, J.; Vučković, J. Nanophotonic computational design. *Opt. Express* **2013**, *21*, 13351 – 13367.
- (12) Niederberger, A. C. R.; Fattal, D. A.; Gauger, N. R.; Fan, S.; Beausoleil, R. G. Sensitivity analysis and optimization of sub-wavelength optical gratings using adjoints. *Opt. Express* **2014**, *22*, 12971 – 12981.
- (13) Piggott, A. Y.; Lu, J.; Lagoudakis, K. G.; Petykiewicz, J.; Babinec, T. M.; Vučković, J. Inverse design and demonstration of a compact and broadband on-chip wavelength demultiplexer. *Nature Photonics* **2015**, *9*, 374–377.
- (14) Frellsen, L. F.; Ding, Y.; Sigmund, O.; Frandsen, L. H. Topology optimized mode multiplexing in silicon-on-insulator photonic wire waveguides. *Opt. Express* **2016**, *24*, 16866 – 16873.
- (15) Sell, D.; Yang, J.; Doshay, S.; Yang, R.; Fan, J. A. Large-angle, multifunctional meta-gratings based on freeform multimode geometries. *Nano letters* **2017**, *17*, 3752–3757.
- (16) Michaels, A.; Yablonovitch, E. Inverse design of near unity efficiency perfectly vertical grating couplers. *Opt. Express* **2018**, *26*, 4766–4779.

- (17) Molesky, S.; Lin, Z.; Piggott, A. Y.; Jin, W.; Vucković, J.; Rodriguez, A. W. Inverse design in nanophotonics. *Nature Photonics* **2018**, *12*, 659.
- (18) Piggott, A. Y.; Petykiewicz, J.; Su, L.; Vučković, J. Fabrication-constrained nanophotonic inverse design. *Sci. Rep.* **2017**, *7*, 1786.
- (19) Su, L.; Piggott, A. Y.; Sapra, N. V.; Petykiewicz, J.; Vučković, J. Inverse Design and Demonstration of a Compact on-Chip Narrowband Three-Channel Wavelength Demultiplexer. *ACS Photonics* **2018**, *5*, 301–305.
- (20) Dory, C.; Vercruysse, D.; Yang, K. Y.; Sapra, N. V.; Rugar, A. E.; Sun, S.; Lukin, D. M.; Piggott, A. Y.; Zhang, J. L.; Radulaski, M.; Lagoudakis, K. G.; Su, L.; Vučković, J. Inverse-designed diamond photonics. *Nature Communications* **2019**, *10*, 3309.
- (21) Hoffman, G. B.; Dallo, C.; Starbuck, A.; Hood, D.; Pomerene, A.; Trotter, D.; DeRose, C. T. Improved broadband performance of an adjoint shape optimized waveguide crossing using a Levenberg-Marquardt update. *Optics Express* **2019**, *27*, 24765–24780.
- (22) Mak, J. C.; Sideris, C.; Jeong, J.; Hajimiri, A.; Poon, J. K. Binary particle swarm optimized 2×2 power splitters in a standard foundry silicon photonic platform. *Optics letters* **2016**, *41*, 3868–3871.
- (23) Fahrenkopf, N. M.; McDonough, C.; Leake, G. L.; Su, Z.; Timurdogan, E.; Coolbaugh, D. D. The AIM Photonics MPW: A Highly Accessible Cutting Edge Technology for Rapid Prototyping of Photonic Integrated Circuits. *IEEE Journal of Selected Topics in Quantum Electronics* **2019**, *25*, 1–6.
- (24) Piggott, A. Y. Automated design of photonic devices. Ph.D. thesis, Stanford University, 2018.

- (25) Giles, M. B.; Pierce, N. A. An Introduction to the Adjoint Approach to Design. *Flow, Turbulence and Combustion* **2000**, *65*, 393–415.
- (26) Johnson, S. G. Notes on Adjoint Methods for 18.335. 2012; <http://math.mit.edu/~stevenj/18.336/adjoint.pdf>.
- (27) Osher, S.; Fedkiw, R. *Level Set Methods and Dynamic Implicit Surfaces*; Springer: New York, U.S.A., 2003.
- (28) Shin, W.; Fan, S. Choice of the perfectly matched layer boundary condition for frequency-domain Maxwell's equations solvers. *J. Comput. Phys.* **2012**, *231*, 3406 – 3431.
- (29) Shin, W.; Fan, S. Accelerated solution of the frequency-domain Maxwell's equations by engineering the eigenvalue distribution. *Opt. Express* **2013**, *21*, 22578 – 22595.
- (30) Lumerical Inc., FDTD: 3D Electromagnetic Simulator. <https://www.lumerical.com/products/>.
- (31) Totzeck, M.; Ulrich, W.; Göhnermeier, A.; Kaiser, W. Pushing deep ultraviolet lithography to its limits. *Nature Photonics* **2007**, *1*, 629.

Graphical TOC Entry

